J. Fluid Mech. (2011), *vol.* 685, *pp.* 365–376.
doi:10.1017/jfm.2011.320

Turbulent spots in oscillatory boundary layers

Marco Mazzuoli, Giovanna Vittori† and Paolo Blondeaux

Department of Civil, Environmental and Architectural Engineering, University of Genoa, 16145, Genoa, Italy

(Received 9 February 2011; revised 19 June 2011; accepted 22 July 2011;
first published online 19 September 2011)

Detailed knowledge of the dynamics of vortex structures in an oscillatory boundary layer is essential for the correct modelling of transport processes in many engineering problems and, in particular, of the pick-up and transport of sediments at the bottom of sea waves. In the present contribution, the formation of turbulent spots in an oscillatory boundary layer is investigated by means of direct numerical simulations. Two of the laboratory experiments of Carstensen, Sumer and Fredsøe are reproduced and, after a comparison of the numerical results with laboratory measurements, a detailed and quantitative characterization of the turbulent spots is also given on the basis of further simulations. The speeds of the head (u_{1H}) and tail (u_{1T}) of the spots are found to scale with the instantaneous free stream velocity U_e and to be similar to those observed in steady boundary layers. The ratios u_{1H}/U_e and u_{1T}/U_e seem to increase with the Reynolds number (R_δ) while the streamwise expansion rate of the spots appears to be independent of R_δ.

Key words: transition to turbulence

1. Introduction

Sediment transport induced by sea waves plays a central role in any morphodynamic phenomenon of the coastal region. Although different approaches exist to evaluate the sediment transport rate at the bottom of sea waves, the actual knowledge of the dynamics of the sediment in the oscillatory boundary layer generated by sea waves does not allow an accurate estimate of the sediment flux. Indeed, even though advanced models are used to evaluate the turbulence structure and sediment dynamics, the results obtained by applying different models disagree and often none of the models provide reliable values of the sediment concentration far from the bottom (Davies *et al.* 1997). In particular, the models find it hard to reproduce the convective events which take place at flow reversal and pick up the sediment from the bottom and carry it into suspension (Ribberink & Al-Salem 1995). In order to improve the predictions of sediment dynamics, it is thus evident that it is necessary to have an accurate description of the dynamics of both the large-scale vortex structures which are generated by the instability of the laminar flow and the small-scale turbulent eddies which are originated by the breakdown of the coherent vortex structures.

A first attempt to experimentally investigate turbulence structure at moderate values of the Reynolds number R_δ was made by Fishler & Brodkey (1991) who, by following

† Email address for correspondence: vittori@dicat.unige.it

suspended tracer particles in the fluid, observed large vortex structures occurring randomly in space but always near or subsequent to the beginning of the decelerating phases. Herein, the Reynolds number R_δ is defined using the amplitude U_0^* of the velocity oscillations just outside the boundary layer and its conventional thickness δ^* equal to $\sqrt{2\nu^*/\omega^*}$, where ω^* is the angular frequency of fluid oscillations, ν^* is the kinematic viscosity of the fluid and an asterisk is used to indicate dimensional quantities. For low values of R_δ, Sarpkaya (1993) observed the formation of unevenly spaced streaks which emerged toward the end of each decelerating phase and then completely disappeared during the accelerating phase. For larger values of R_δ, the streaks interacted, moving towards each other and growing in amplitude and, then, split into short segments which, in turn, began to lift. For Reynolds numbers in the range 460–490, a larger number of vortices appeared towards the end of the decelerating phases, and as R_δ was increased, more numerous vortex structures formed, which penetrated further into the ambient flow.

The experimental evidence of the formation of coherent vortex structures in oscillatory boundary layers was confirmed also by numerical simulations. Costamagna, Vittori & Blondeaux (2003) investigated an oscillatory boundary layer with the aim of isolating the basic flow unit and studying wall turbulence in the near-wall region. They observed a sequence of events similar to those detected in steady boundary layers and, in particular, towards the end of the accelerating phases they observed the formation of high- and low-speed streaks with spacing and characteristics similar to those of steady boundary layers. Then, the high- and low-speed streaks, located close to the wall, twisted, interacted and broke producing small vortices which dissipated due to viscous effects.

Recently, Carstensen, Sumer & Fredsøe (2010) performed laboratory experiments for a wide range of values of R_δ. They observed two kind of flow structures in the transitional regime: vortex tubes and turbulent spots. Vortex tubes are two-dimensional vortices, with horizontal axes orthogonal to flow direction which are observed for R_δ ranging from 374 to 775. For values of R_δ larger than 548, Carstensen *et al.* (2010) also observed turbulent spots which are isolated turbulent areas close to the wall in an otherwise laminar boundary layer and cause violent velocity and shear stress oscillations. They observed that turbulent spots emerge from the dynamics of streaks which develop twisting and turning motions and then break into smaller structures, which give rise to arrowhead-shaped turbulent spots. Since Emmons (1951) observed the formation of turbulent spots in a laminar boundary layer undergoing transition, many results have appeared in the literature on the characterization of turbulent spots. However, all of the investigations of turbulent spots consider steady flows and Carstensen *et al.* (2010) were the first to observe turbulent spots in an unsteady oscillatory flow.

In the present paper the results of the direct numerical simulation (DNS) of an oscillating boundary layer are presented in order to fill the gap between the results of Costamagna *et al.* (2003) and the more recent observations of Carstensen *et al.* (2010). In particular, new DNSs, which reproduce two tests of Carstensen *et al.* (2010) as well as a third run for a larger value of R_δ, are presented. The results show the formation of turbulent spots, after the break-up of the high- and low-speed streaks. After a detailed comparison of the numerical findings with the experimental measurements of Carstensen *et al.* (2010), the characteristics of turbulent spots are investigated both qualitatively and quantitatively.

2. The problem and the numerical approach

If the linear Stokes wave theory is used to describe the inviscid irrotational flow generated by the propagation of a monochromatic sea wave, the flow in the bottom boundary layer can be studied by determining the flow generated close to the bed by an oscillating pressure gradient described by

$$\frac{\partial P^*}{\partial x_1^*} = -\rho^* U_0^* \omega^* \sin(\omega^* t^*); \quad \frac{\partial P^*}{\partial x_2^*} = 0; \quad \frac{\partial P^*}{\partial x_3^*} = 0, \tag{2.1}$$

where (x_1^*, x_2^*, x_3^*) is a Cartesian coordinate system with the x_1^*-axis pointing in the direction of wave propagation, the x_2^*-axis is vertical and pointing in the upward direction such that $x_2^* = 0$ describes the averaged bottom location. As in Blondeaux & Vittori (1994) and Costamagna *et al.* (2003), we consider a wall characterized by a small waviness such that its profile η^* is given by the superimposition of sinusoidal components

$$x_2^* = \epsilon^* \eta(x_1^*, x_3^*) = \epsilon^* \sum_{n=1}^{N} a_n \cos(\alpha_n^* x_1^* + \gamma_n^* x_3^* + \varphi_n), \tag{2.2}$$

where $\epsilon^* a_n$ denotes the amplitude of the nth component, which is characterized by wavenumbers α_n^* and γ_n^* in the x_1^* and x_3^* directions, respectively, and by a phase φ_n. In the present simulations, ϵ^* is taken equal to $0.005\delta^*$, which, considering typical values of δ^*, corresponds to a waviness of the bottom profile which cannot be appreciated from the macroscopic point of view. Moreover, for the chosen values of the parameters appearing in (2.2) (see table 1), the ratio between the amplitude and the characteristic wavelength of the bottom waviness is of order $O(10^{-4})$, making the wall imperfection quite different from a typical roughness. As discussed by Vittori & Verzicco (1998), the characteristics of turbulence, which appears when the laminar flow turns out to be unstable, are not affected by the values of N, a_n, α_n and γ_n as long as the bottom can be assumed smooth from a macroscopic point of view.

The Navier–Stokes and continuity equations in non-dimensional form read:

$$\frac{\partial u_i}{\partial t} + \frac{R_\delta}{2} u_j \frac{\partial u_i}{\partial x_j} = -\frac{R_\delta}{2} \frac{\partial p}{\partial x_i} - \delta_{i1} \sin(t) + \frac{1}{2} \frac{\partial^2 u_i}{\partial x_k \partial x_k}; \quad \frac{\partial u_j}{\partial x_j} = 0; \quad i = 1, 2, 3, \tag{2.3}$$

where the following non-dimensional variables are used:

$$\left.\begin{aligned} t = t^* \omega^*; \quad (x_1, x_2, x_3) &= \frac{(x_1^*, x_2^*, x_3^*)}{\delta^*}; \\ (u_1, u_2, u_3) = \frac{(u_1^*, u_2^*, u_3^*)}{U_0^*}; \quad p &= \frac{p^*}{\rho^* (U_0^*)^2} \end{aligned}\right\} \tag{2.4}$$

where t^* denotes time, p^* denotes pressure and u_1^*, u_2^*, u_3^* denote the fluid velocity components along the x_1^*, x_2^* and x_3^* directions, respectively. The equations are solved numerically in a computational domain of dimensions L_{x1}, L_{x2} and L_{x3} in the streamwise, cross-stream and spanwise directions, respectively. At the wall, having assumed the amplitude of the wall waviness to be much smaller than the thickness of the laminar boundary layer ($\epsilon = \epsilon^*/\delta^* \ll 1$), the no-slip condition is expanded up to second order in the variable ϵ and it is forced at $x_2 = 0$ (see Vittori & Verzicco 1998). The numerical scheme is second-order accurate in space and in all of the simulations ϵ has been taken to be smaller than the size of the first computational grid in the x_2 direction. As a consequence, the approximation of the

no-slip condition is consistent with the accuracy of the numerical method employed to solve (2.3). At the upper boundary of the computational domain, a symmetry condition is forced, which is equivalent to require the vanishing of tangential stresses far from the wall and to impose that the velocity tends to $(-U_0^* \cos \omega^* t^*, 0, 0)$. Moreover, the turbulent flow is assumed to be homogeneous in the streamwise and spanwise directions and periodic boundary conditions are thus forced along the x_1- and x_3-axes. The computational mesh is uniform in the streamwise and spanwise directions while in the cross-stream direction a non-uniform mesh is used to cluster the grid points in the vicinity of the wall where velocity gradients are expected to be larger. The minimum and maximum values of the grid size in the cross-stream direction are 0.16 and 0.59, respectively. The numerical approach uses standard centred second-order finite difference approximations of the spatial derivatives, while the time advancement of Navier–Stokes equations is made using the fractional-step method. Details of the procedure are given by Orlandi (1989), Vittori & Verzicco (1998) and Costamagna *et al.* (2003), where a quantitative comparison is also made between the numerical results and the experimental measurements of Jensen, Sumer & Fredsoe (1989). In Costamagna *et al.* (2003) a computational box of size equal to $L_{x1}^* = 25.13\delta^*$, $L_{x2}^* = 25.13\delta^*$ and $L_{x3}^* = 12.57\delta^*$ in the streamwise, vertical and spanwise directions, respectively, was used. However, the experiments of Carstensen *et al.* (2010) show the formation of turbulent spots which, during their evolution, have a size larger than that of the computational box of Costamagna *et al.* (2003). Indeed, figure 9 of Carstensen *et al.* (2010) shows the formation of a turbulent spot of size comparable to the size of the picture area, which is approximately equal to 38 cm $\times$ 13 cm in the streamwise and spanwise directions, respectively and, hence, $218\delta^*$ long and $76\delta^*$ large. It turns out that the displayed area for test 6 of Carstensen *et al.* (2010) is 9.5 times larger in the streamwise direction and 6 times larger in the spanwise directions with respect to that considered by Costamagna *et al.* (2003). Hence, in present simulations the box size has been increased, and the number of computational points (n_1, n_2 and n_3 in the x_1, x_2 and x_3 directions, respectively) has been increased consequently, in order to have an accurate reproduction of the tests 6 and 7 of Carstensen *et al.* (2010). Then, a further run is made to extend the range of the Reynolds number presently investigated. By computing the fast Fourier transform (FFT) of the velocity field, it has been verified that the spatial resolution is adequate in the x_1 and x_3 directions since at each time the amplitude of the spectral components with the largest wavenumbers is smaller than a few per cent of the maximum amplitude.

Moreover, a few runs made with more points in the vertical direction have shown that the vertical resolution is also adequate. The values of the numerical parameters for each run are given in table 1.

3. Discussion of the results

3.1. *Comparison with the experimental measurements of Carstensen et al. (2010)*

During their experiments in the transitional regime, Carstensen *et al.* (2010) detected two types of coherent flow structures: vortex tubes and turbulent spots. Vortex tubes are two-dimensional vortices close to the bed which extend across the width of the flow in a plane view. Turbulent spots, which appear randomly in space, are isolated areas close to the bed where the flow velocity and wall shear stress show violent oscillations, in an otherwise laminar flow. Figure 1 shows the bed shear stress presently computed for values of the parameters chosen to reproduce the fourth half-cycle of experiment 6 of Carstensen *et al.* (2010), along with the value

(*a*)	Test n	R_δ	L_{x1}	L_{x2}	L_{x3}	n_1	n_2	n_3	n
	T1	948	213.60	25.13	75.40	541	65	385	2
	T2	775	226.19	25.13	94.25	572	65	480	2
	T3	1220	213.60	25.13	75.40	541	65	385	2

(*b*)	Test n	a_1	a_2	α_1	α_2	γ_1	γ_2	φ_1	φ_2
	T1	1	0.1	0.5	0	0	1	0	0
	T2	1	0.1	0.5	0	0	1	0	0
	T3	1	0.1	0.5	0	0	1	0	0

TABLE 1. Numerical parameters of the present simulations. Here $\alpha_n = \alpha_n^* \delta^*$ and $\gamma_n = \gamma_n^* \delta^*$.

of $|\tau_0^*|/\rho^*$ measured by Carstensen *et al.* (2010) and shown in figure 14 of their paper. Figure 1 shows the dimensional quantity τ_0^*/ρ^* at different positions along the central streamwise line: the presence of spikes, which are related by Carstensen *et al.* (2010) to the presence of turbulent spots passing the measuring point, can be recognized both in the computed and measured values. It can be also observed that, because of the randomness of the location where the turbulent spots appear as well as because of the large variability in their intensity, the turbulent fluctuations of the bottom shear stress are characterized by a large variability from location to location and from cycle to cycle. Even though the time development of the bottom shear stress shows differences as the measuring position is varied, the numerical values qualitatively agree with the measurements by Carstensen *et al.* (2010) which give the shear stress averaged over the area of the measuring probe. Figure 2 shows the modulus of the fluctuating part of the bed shear stress for test T1, which is characterized by the same Reynolds number as the fourth half-oscillating cycle of tests 6 of Carstensen *et al.* (2010). The numerical results shown in figure 2 should be compared with figures 9 and 13 of Carstensen *et al.* (2010). It is worth recalling that the size of the computed (and displayed) area (presently expressed in non-dimensional units) corresponds to that shown in figure 9 of Carstensen *et al.* (2010). Similarly to Carstensen *et al.* (2010), turbulent spots appear randomly in space towards the end of the accelerating phases and grow in intensity and size until, at the early stage of the decelerating phases, they pervade the whole boundary layer. Later on, during the early stage of the following accelerating phases, turbulence decays and the flow tends to recover a laminar-like behaviour.

3.2. *Turbulent spots*

To quantify the geometric characteristics of the turbulent spots, a quantitative analysis was performed for a large number of spots, before they merge with their neighbours. A preliminary analysis aimed at choosing the criterion to detect the boundaries of the spots was made. The boundaries of a spot were defined and detected as the boundaries of the area where an appropriate quantity exceeds a fixed value. We considered: (i) the local value of the dimensionless production of turbulent kinetic energy (TKEP), (ii) the local value of the dimensionless turbulent kinetic energy (TKE), (iii) the modulus of the projection on a horizontal plane of the fluctuating component of the dimensionless shear stress ($|\tau'|$), (iv) the absolute value of the fluctuating component of the dimensionless streamwise velocity ($|u_1'|$), (v) the absolute value of the fluctuating component of the dimensionless spanwise velocity ($|u_3'|$) . The threshold values used in this comparison were fixed equal to a few per cent of the maximum in time and space of the chosen quantity. Incidentally, let us point out that

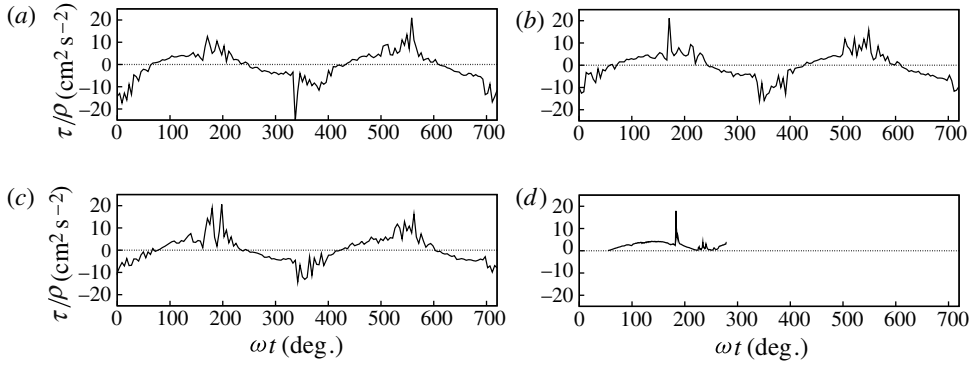

FIGURE 1. Time development of the streamwise component of the wall shear stress for test T1, corresponding to the fourth half cycle of Carstensen *et al.* (2010). The different panels show the results at different positions along the central streamwise line: (*a*) $x_1 = 39.5$; (*b*) $x_1 = 79.11$; (*c*) $x_1 = 197.8$. Panel (*d*) shows the experimental data by Carstensen *et al.* (2010).

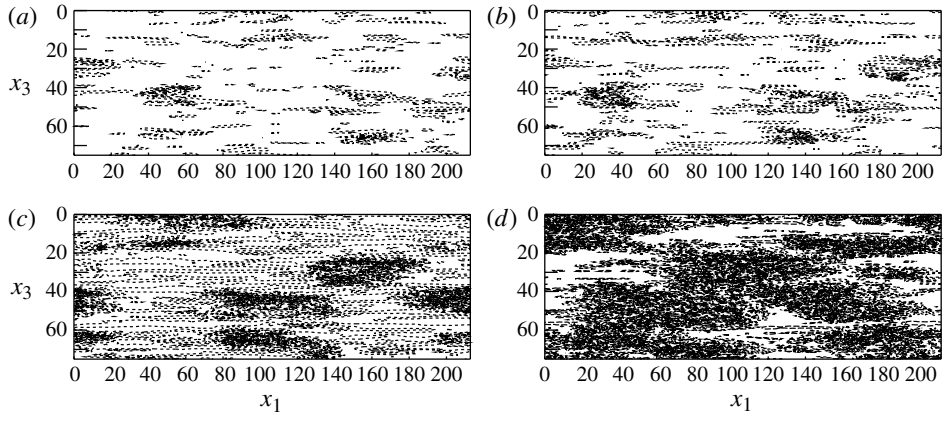

FIGURE 2. Modulus of the fluctuating part of the bottom shear stress $\overline{\tau}_o$. First isoline $\overline{\tau}_o = 0.2$, isoline interval = 0.5; (*a*) $t = 11.78$; (*b*) $t = 11.86$; (*c*) $t = 12.02$; (*d*) $t = 12.17$. The free stream velocity is directed from the right to the left. Values of the parameters chosen to reproduce the fourth half-oscillation cycle of test 6 of Carstensen *et al.* (2010).

Criterion	x_{1Head}	x_{1Tail}	u_{1H}	u_{1T}
TKEP	50.24	77.53	−0.77	−0.56
TKE	50.24	77.53	−0.75	−0.55
$\lvert\tau'\rvert$	52.21	73.57	−0.80	−0.55
$\lvert u_1'\rvert$	50.24	77.13	−0.75	−0.55
$\lvert u_3'\rvert$	52.31	71.73	−0.77	−0.54

TABLE 2. Position of the head and tail of turbulent spot A (see figure 3*a*) at $t = 5.653$ and $x_2 = 0.2355$ and their average speeds for $5.5 \leqslant t \leqslant 5.7$ computed using the different criteria defined in the text (Test T1).

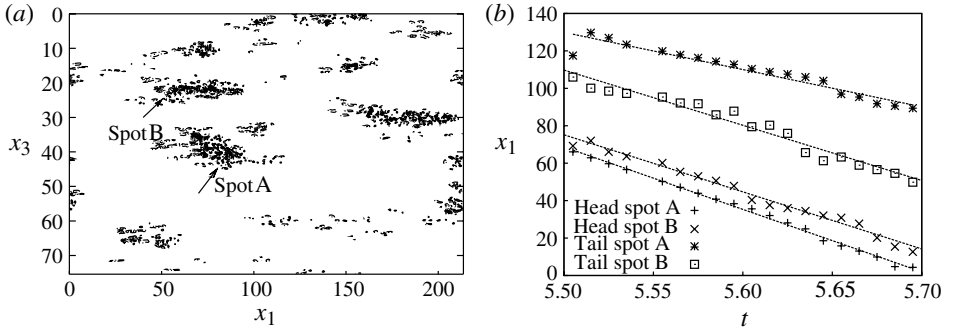

FIGURE 3. (*a*) TKEP at $t = 5.575$, $x_2 = 0.24$, $\Delta_{TKEP} = 0.005R_\delta$; (*b*) position of the head and tail of spot A and spot B, identified by means of the TKEP criterion, plotted versus time. The lines have been obtained by linear regression. The outer flow is directed from right to left. Test T1.

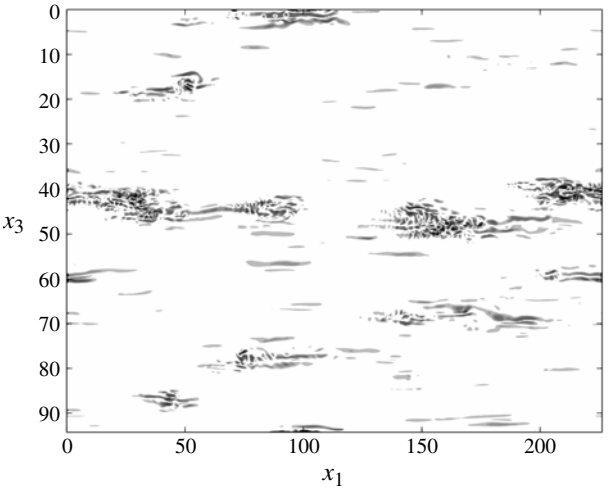

FIGURE 4. TKEP in the plane x_1–x_3 at $x_2 = 0.4$, $t = 15.28$, Test T2. Here $\mathrm{TKEP}_{min} = 1.2 \times 10^{-11}R_\delta$ and $\mathrm{TKEP}_{max} = 0.0188R_\delta$. The outer flow is directed from left to right.

the TKEP term in the dimensionless turbulent kinetic energy equation, turns out to be proportional to R_δ. The detection of the time development of the boundaries of the spot makes it possible to evaluate their velocity. Figure 3(*b*) shows the evolution of the positions of the head and tail of spots A and B which are first detected during test T1 at $t = 5.3$ and start to merge with their neighbours at $t = 5.8$. The lines indicate the least-squares fit of the data and approximate the actual positions of the head and tail of the spots with a root mean square (r.m.s.) error which ranges between $1.13\delta^*$ and $3.33\delta^*$. Therefore, it can be concluded that, during the time interval considered, the speed of the head and tail of the spots can be assumed to be practically constant and given by the slope of each line. Table 2 shows the outputs of the analysis performed by means of the different criteria and allows to conclude that, even though differences exist when different quantities are considered, the differences are small as far as the location of the head/tail of the spot is concerned. Moreover, the evaluation of the

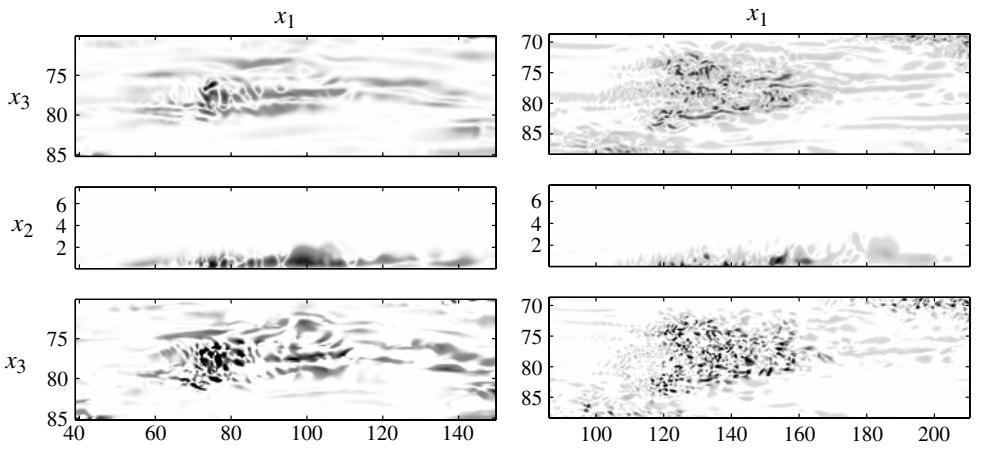

FIGURE 5. TKEP in the plane x_1–x_3 at $x_2 = 0.4$ (top row) and in the plane x_1–x_2 at $x_3 = 77.13$ (middle row). The bottom row shows the vortex structures in the plane x_1–x_3 at $x_2 = 0.4$ identified by means of the λ_2 criterion (Jeong & Hussain 1995). Left column, $t = 15.28$, $\mathrm{TKEP}_{min} = 2.45 \times 10^{-11} R_\delta$, $\mathrm{TKEP}_{max} = 0.0051 R_\delta$, $\lambda_{2min} = -0.0111$, $\lambda_{2max} = 0$; right column, $t = 15.51$, $\mathrm{TKEP}_{min} = 0.88 \times 10^{-9} R_\delta$, $\mathrm{TKEP}_{max} = 0.0127 R_\delta$, $\lambda_{2min} = -0.0894$, $\lambda_{2max} = 0$. The outer flow is directed from left to right. Test T2.

speed of the head and tail of the spot with the different methods shows values which differ by at most a few per cent. On the basis of this preliminary investigation, it was chosen to identify the boundaries of the turbulent spots by using the TKEP criterion. A visual analysis of many spots shows that, differently from the steady boundary layer in which an isolated spot is excited (Schubauer & Klebanoff 1955; Singer 1996) and similarly to the laboratory observations of Carstensen *et al.* (2010), the naturally forming spots in the present flow show no general form. Moreover, figure 4 shows that the presence of many spots often makes it difficult to distinguish one spot from the other and in many cases the form of a spot appears to be influenced by its neighbours. However, the spots which are detached from the others often show an arrow-like form. Moreover, a general characteristic of the spots, observed at the early stages of their formation, is the presence of longitudinal vortices located at the sides of the spot itself. These vortices, which can be clearly seen in the top row of figure 5, are also detected by means of the λ_2 criterion, proposed by Jeong & Hussain (1995) to identify vortex structures (see figure 5, bottom row). It is observed that two vortices are located upstream of the head and two lateral structures follow the spot. Moreover, quite often, transversal wave-like structures are observed. The vertical section of the spot shows that the leading streamwise vortices are inclined with respect to the wall (see figure 5, middle row). At later times, when the turbulent spot becomes mature, the system of vortices is no longer recognizable (figure 5, right panels). Many spots appearing during different cycles, were followed during their evolution and the dimensionless speeds of the head (u_{1H}), tail (u_{1T}), left side (u_{3LS}) and right side (u_{3RS}) were computed for different distances from the wall. Figure 6(*a*) shows the speeds computed for two spots which form during the third half-oscillation cycle of T2. The vertical distribution of the speeds shows some oscillations, presumably related to the difficulties in accurately estimating the position of the borders of the spots. However, these oscillations can be neglected and in the following only the speeds averaged in the x_2 direction are presented. Differences are found if spots at different cycles are considered (see

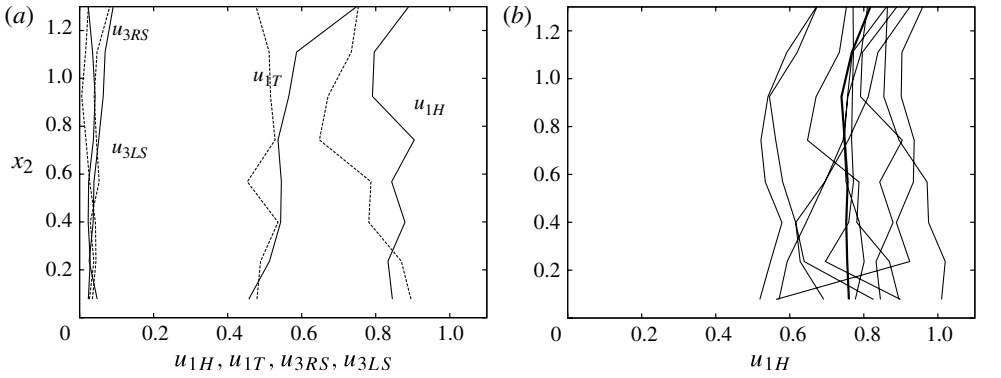

FIGURE 6. (*a*) Speeds of the head (u_{1H}), tail (u_{1T}), left side (u_{3LS}) and right side (u_{3RS}) for two spots in the third oscillating cycle as function of the vertical coordinate x_2. (*b*) Speeds of the head of different spots at different half cycles together with the average value (thick solid line) as a function of the vertical coordinate (Test T2).

figure 6*b*). These differences might be partially due to a possible correlation between the velocity of the boundaries of the spots with the external velocity which is different because the spots appear at slightly different phases in the cycle.

Table 3 gives the average speeds of the spots for the three runs. Columns 3–6 show u_{1H}, u_{1T}, u_{3LS} and u_{3RS} while the remaining columns show the corresponding quantities scaled with the instantaneous value of the outer velocity $U_e^*((\hat{u}_{1H}, \hat{u}_{1T}, \hat{u}_{3LS}, \hat{u}_{3RS}) = (u_{1H}^*, u_{1T}^*, u_{3LS}^*, u_{3RS}^*)/U_e^*)$. Even though the speeds are given with two significant digits, the second digit should be treated with caution.

The speed of the spots is smaller than the external velocity, in accordance with results for steady boundary layers (Schubauer & Klebanoff 1955; Singer 1996). For the Blasius boundary layer Schubauer & Klebanoff (1955), by means of an experimental investigation of the characteristics of a turbulent spot artificially initiated, detected values of the head and tail of the spot equal to $0.88U_e^*$ and $0.5U_e^*$, respectively. A numerical investigation of a spot, initiated in a Blasius boundary layer by a localized disturbance, showed values of the speed of the head and tail of the spot equal to $0.97U_e^*$ and $0.63U_e^*$, respectively (Singer 1996). Thus, it appears that, even though the present boundary layer is unsteady, the speeds of the head and tail of the spots, normalized with the instantaneous actual velocity, are similar to those detected in steady boundary layers. The speeds of the two lateral boundaries of the spot are one order of magnitude smaller than those of the head and tail because they are due to turbulent diffusion only. Similar values of $\hat{u}_{3LS}$ and $\hat{u}_{3RS}$ are obtained for T1, T2 and T3, while a significant difference is found for $\hat{u}_{1H}$ and $\hat{u}_{1T}$. Indeed, even though the values of u_{1H} and u_{1T} are practically constant when R_δ is increased from 775 to 948 (the reader should consider the uncertainty in the second digit), a further increase of R_δ leads to a significant decrease of both u_{1H} and u_{1T}. Moreover, a monotonic growth of $\hat{u}_{1H}$ and $\hat{u}_{1T}$ is observed as R_δ is increased and for run T3 ($R_\delta = 1220$), u_{1H} and u_{1T} are larger than those for run T2 ($R_\delta = 775$) of approximately 20–30 %. The growth of $\hat{u}_{1H}$ and $\hat{u}_{1T}$ with R_δ is related to an earlier appearance of turbulence during the accelerating phase and to the consequent decrease of U_e^*. Finally, it can be appreciated that the expansion rate of the spot in the streamwise direction is significantly larger than that in the spanwise direction even though they do not appear to significantly depend on the Reynolds number.

Test n	R_δ	u_{1H}	u_{1T}	u_{3LS}	u_{3RS}	$\hat{u}_{1H}$	$\hat{u}_{1T}$	$\hat{u}_{3LS}$	$\hat{u}_{3RS}$
T1	948	0.68	0.41	0.02	0.03	0.87	0.53	0.03	0.04
T2	775	0.67	0.40	0.04	0.03	0.78	0.46	0.04	0.03
T3	1220	0.51	0.33	0.02	0.03	0.94	0.61	0.04	0.05

TABLE 3. Speed of the head of the spot (u_{1H}), tail of the spot (u_{1T}), right side of the spot (u_{3RS}) and left side of the spot (u_{3LS}). The caret indicates the speed scaled with the instantaneous outer flow.

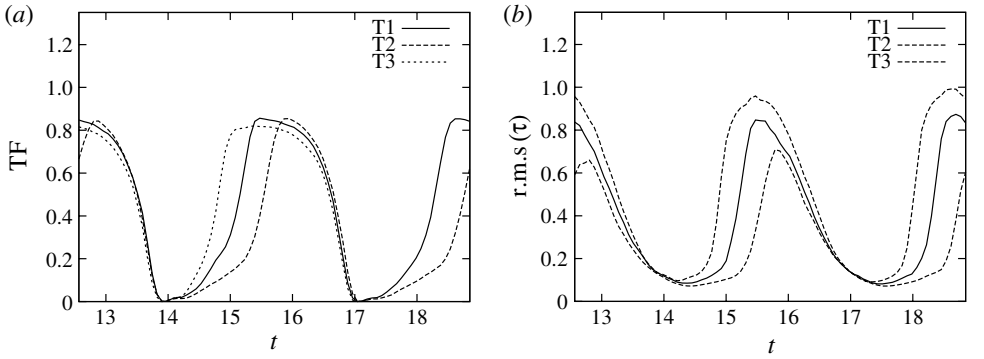

FIGURE 7. (*a*) TF versus time at $x_2 = 0.24$; (*b*) r.m.s. of the bottom shear stress oscillations versus time.

In order to quantify the area of the computational domain which is under the influence of turbulent spots, the turbulent fraction (TF) is considered. The TF is the ratio of the area, for a fixed value of x_2, where TKEP exceeds an assigned value P_t ($P_t = 0.5 \times 10^{-4} R_\delta$) and the total area ($L_{x1} \times L_{x3}$). Even though the value of TF depends on P_t, its qualitative time development, which is analysed in the following, is not affected.

At this stage it is worthwhile to recall that the characteristics of the turbulent spots have been obtained by means of the TKEP criterion; therefore TF appears to be the most natural quantity to use in order to obtain global information on the time evolution of turbulent spots. Figure 7, where the value of TF is plotted versus time, shows that the turbulent production starts to grow considerably during the accelerating phases as in the visual observations of Fishler & Brodkey (1991) and the comparable tests in the recent experiments of Carstensen *et al.* (2010). TF reaches a maximum value near the end of the accelerating phases when turbulence pervades the whole area. Then TF remains almost constant over a time interval which depends on R_δ and it is significant for the largest R_δ ($R_\delta = 1220$) while it is negligible for $R_\delta = 775$. Finally the area with significant levels of turbulence production decreases. Hence, the numerical simulations confirm that turbulence appears during the late accelerating phases of the cycle and reaches the maximum intensity at about the end of the accelerating phases or during the decelerating phases. Moreover, figure 7 shows that the growth of TF and its maximum take place earlier if the value of R_δ is increased. During the early stages of TF growth, when turbulent spots are detached from each other, TF is related to the average area of each spot times the number of spots. When turbulent spots merge no information can be obtained from TF and other quantities should be considered to investigate turbulence structure. For example the

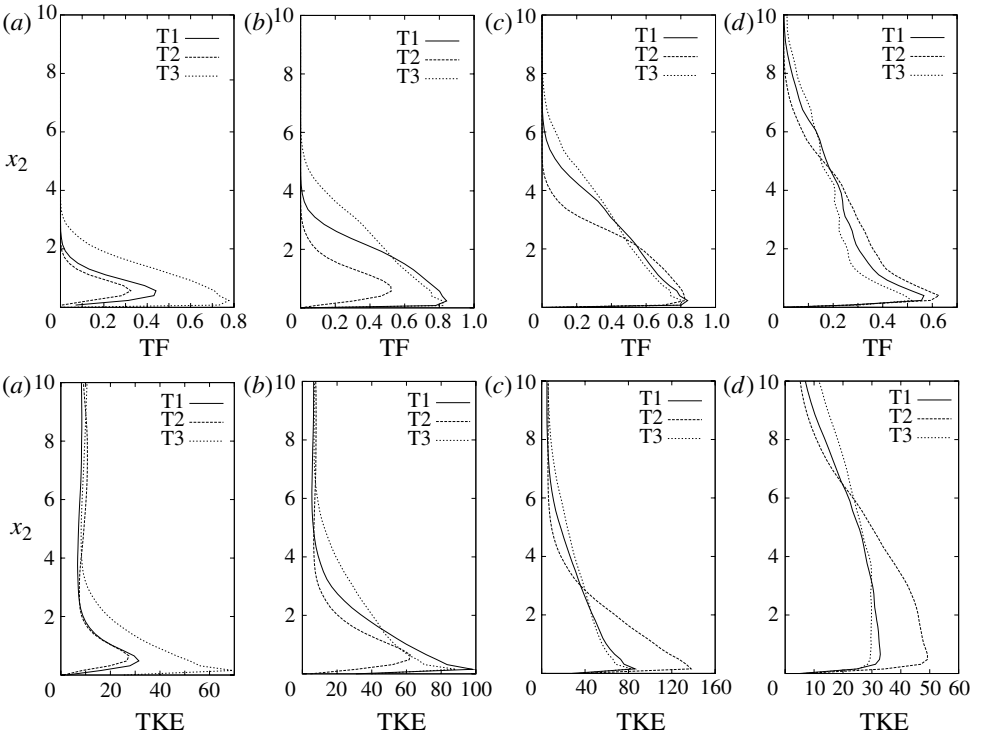

FIGURE 8. First row: TF versus x_2. Second row: turbulent kinetic energy versus x_2. (*a*) $t = 15$; (*b*) $t = 15.39$; (*c*) $t = 15.79$; (*d*) $t = 16.57$.

r.m.s. value of the bed shear stress oscillations, which is plotted in figure 7(*b*), shows that turbulence intensity grows as R_δ is increased and turbulence affects a larger part of the oscillating cycle. Finally, figure 8 (first row) shows that the maximum of TF takes place at a similar distance from the wall for the three runs, indicating that the location of the maximum of turbulent kinetic energy production does not significantly depend on R_δ. Even though negligible values of TF are found for x_2 larger than about $10\delta^*$, figure 8 (second row) shows that turbulence is present and significant at larger distances, because of turbulence diffusion. Hence, the boundary layer thickness turns out to be larger than the region where turbulence is produced.

4. Conclusions

The results of DNSs of an oscillatory boundary layer confirm the experimental findings of Carstensen *et al.* (2010). In the range of the Reynolds numbers presently investigated, turbulent spots, which are turbulent areas in an otherwise laminar boundary layer, appear near the end of the accelerating phases and cause spikes in the wall shear stress and velocity field. Later, turbulence pervades the whole boundary layer and causes large values of the bottom shear stress over the whole bottom. Since DNS gives access to velocity and pressure fields in the three-dimensional space and time, the numerical simulations supplement the investigation carried out by Carstensen *et al.* (2010). Indeed they allow new quantities to be obtained. In particular, the speed of the head and tail of the spots can be determined along with the speed of the lateral spreading of the spot. Even though the flow is highly unsteady, the speeds turn

out to be similar to those found in steady boundary layers. Indeed the speed of the head falls between $0.78U_e^*$ and $0.94U_e^*$ and that of the tail ranges between $0.46U_e^*$ and $0.61U_e^*$, where U_e^* is the instantaneous external free stream velocity. Finally, the speed of the lateral boundaries turns out to range between $0.03U_e^*$ and $0.05U_e^*$. The averaged bottom shear stress rapidly increases when turbulent spots start to appear. The spatial distribution of τ is uneven and τ is larger under the spots where TKE as well as TKEP are also larger. Hence, the area characterized by large values of the bottom shear stress grows at the same rate of the spots. These results suggest that the interaction of the oscillatory flow with a cohesionless bottom is largely affected by the presence, number and intensity of turbulent spots. In particular, an investigation of the interaction of turbulent spots with the sediment lying on the bottom, to be carried out in the future, might lead to more physically based formulae to determine the inception of sediment transport and to quantify the sediment transport rate.

The authors wish to acknowledge S. Carstensen, B. M. Sumer and J. Fredsøe who provided the experimental data shown in figure 1 and the three anonymous reviewers for their useful comments.

REFERENCES

BLONDEAUX, P. & VITTORI, G. 1994 Wall imperfections as a triggering mechanism for Stokes-layer transition. *J. Fluid Mech.* **264**, 107–135.

CARSTENSEN, S., SUMER, B. M. & FREDSØE, J. 2010 Coherent structures in wave boundary layers. Part 1. Oscillatory motion. *J. Fluid Mech.* **646**, 169–206.

COSTAMAGNA, P., VITTORI, G. & BLONDEAUX, P. 2003 Coherent structures in oscillatory boundary layers. *J. Fluid Mech.* **474**, 1–33.

DAVIES, A. G., RIBBERINKB, J. S., TEMPERVILLE, A. & ZYSERMAN, J. A. 1997 Comparisons between sediment transport models and observations made in wave and current flows above plane beds. *Coast. Engng* **31**, 163–198.

EMMONS, H. 1951 Laminar-turbulent transition in boundary layer. *J. Aeronaut. Sci.* **18** (7), 490–498.

FISHLER, L. S. & BRODKEY, R. S. 1991 Transition, turbulence and oscillating flow in a pipe. *Exp. Fluids* **11**, 388–398.

JENSEN, B. L., SUMER, B. M. & FREDSOE, J. 1989 Turbulent oscillatory boundary layers at high Reynolds numbers. *J. Fluid Mech.* **206**, 265–297.

JEONG, J. & HUSSAIN, F. 1995 On the identification of a vortex. *J. Fluid Mech.* **285**, 67–94.

ORLANDI, P. 1989 A numerical method for direct simulation of turbulence in complex geometries. *Annual Research Brief*, 215. Center for Turbulence Research, Standford University.

RIBBERINK, J. S. & AL-SALEM, A. A. 1995 Sheet flow and suspension of sand in oscillatory boundary layers. *Coast. Engng* **25**, 205–225.

SARPKAYA, T. 1993 Coherent structures in oscillatory boundary layers. *J. Fluid Mech.* **253**, 105–140.

SCHUBAUER, G. B. & KLEBANOFF, P. S. 1955 Contributions on the mechanics of boundary-layer transition. NACA TN-3489.

SINGER, B. A. 1996 Characteristics of a young turbulent spot. *Phys. Fluids* **8** (2), 509–521.

VITTORI, G. 2003 Sediment suspension due to waves. *J. Geophys. Res.* **108** (6), 3173.

VITTORI, G. & VERZICCO, R. 1998 Direct simulation of transition in an oscillatory boundary layer. *J. Fluid Mech.* **371**, 207–232.